

Missing No More: Dictionary-Guided Cross-Modal Image Fusion under Missing Infrared

Yafei Zhang¹, Meng Ma¹, Huafeng Li^{1*}, Yu Liu²,

¹Faculty of Information Engineering and Automation, Kunming University of Science and Technology,

²Department of Biomedical Engineering, Hefei University of Technology

Abstract

Infrared-visible (IR-VIS) image fusion is vital for perception and security, yet most methods rely on the availability of both modalities during training and inference. When the infrared modality is absent, pixel-space generative substitutes become hard to control and inherently lack interpretability. We address missing-IR fusion by proposing a dictionary-guided, coefficient-domain framework built upon a shared convolutional dictionary. The pipeline comprises three key components: (1) Joint Shared-dictionary Representation Learning (JSRL) learns a unified and interpretable atom space shared by both IR and VIS modalities; (2) VIS-Guided IR Inference (VGII) transfers VIS coefficients to pseudo-IR coefficients in the coefficient domain and performs a one-step closed-loop refinement guided by a frozen large language model as a weak semantic prior; and (3) Adaptive Fusion via Representation Inference (AFRI) merges VIS structures and inferred IR cues at the atom level through window attention and convolutional mixing, followed by reconstruction with the shared dictionary. This encode→transfer→fuse→reconstruct pipeline avoids uncontrolled pixel-space generation while ensuring prior preservation within interpretable dictionary-coefficient representation. Experiments under missing-IR settings demonstrate consistent improvements in perceptual quality and downstream detection performance. To our knowledge, this represents the first framework that jointly learns a shared dictionary and performs coefficient-domain inference-fusion to tackle missing-IR fusion. The source code is publicly available at <https://github.com/harukiv/DCMIF>.

1. Introduction

Infrared-visible (IR-VIS) image fusion is critical for robust perception in surveillance, robotics, and autonomous systems. Most existing approaches assume both modalities are available during training and inference, and adopt end-to-end designs—CNNs [18, 20, 45], CNN-Transformer hy-

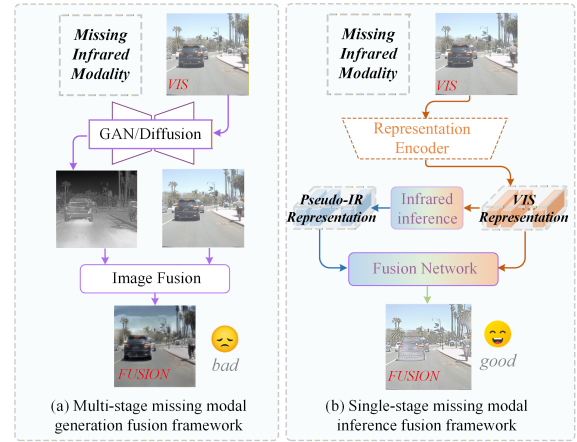


Figure 1. Comparison between existing methods and ours. For infrared-missing cross-modal fusion, (a) existing methods adopt a multi-stage framework that generates infrared images before fusion, while (b) we propose a single-stage framework that directly infers infrared features from visible images without generating infrared images.

brids [19, 31, 34], GANs [21, 32], or diffusion models [48, 50]—to directly regress a fused image from paired inputs. While effective under standard conditions, this assumption often breaks in realistic missing-modality scenarios (e.g., VIS-only at test time). Moreover, pixel-space black-box generation offers weak physical consistency and interpretability, often resulting in unstable thermal cue completion, structural detail loss, or hallucinated patterns.

We address IR-VIS fusion under missing-IR conditions by predicting infrared cues from visible information and fusing them with the visible image, thereby enhancing perceptual quality and improving performance in downstream vision tasks such as object detection and semantic segmentation. As shown in Figure 1, rather than directly generating IR in pixel space, we map both modalities into a unified dictionary-coefficient space to perform interpretable inference and fusion in the coefficient domain, followed by reconstruction using the shared dictionary. This anchors data consistency and prior constraints at the atom-coefficient level, effectively avoiding the brittleness of pixel-space genera-

*Corresponding author: Huafeng Li (hfchina99@163.com)

tion.

To this end, we propose a shared-dictionary, atom-correspondence forecasting framework (Figure 2) composed of three synergistic modules: Joint Shared-dictionary Representation Learning (JSRL), VIS-Guided IR Inference (VGII), and Adaptive Fusion via Representation Inference (AFRI). JSRL learns a cross-modal shared convolutional dictionary that projects IR and VIS onto a common atom space, thereby establishing atom-level correspondences in the dictionary-coefficient space. VGII builds a coefficient-domain transfer from VIS to IR by mapping visible coefficients to pseudo-IR coefficients and applying a lightweight refinement to enhance thermal coverage. AFRI then feeds VIS and predicted IR coefficients into an adaptive fusion network that integrates window attention and convolutional mixing at the atom level. The network outputs fused coefficients, from which the final image is reconstructed using the shared dictionary.

Compared with prior work, our method differs in three substantive ways: (i) modeling and inference are performed entirely in the coefficient domain under a shared dictionary, forming a closed loop of *encode* \rightarrow *transfer* \rightarrow *fuse* \rightarrow *reconstruct* instead of pixel-space black-box generation; (ii) explicit atom-level correspondences render the transfer and fusion processes interpretable; and (iii) a weak semantic prior is introduced via simple linear modulation instead of a heavy generative head, enabling controllable thermal completion with improved stability. As a result, under missing-IR conditions our approach preserves IR target saliency while maintaining VIS structural detail. **Our work makes the first attempt to explore how the image-fusion paradigm can enhance perceptual quality and downstream performance from a single visible image when the infrared modality is missing.** The main contributions are as follows:

- **Dictionary-guided coefficient-domain paradigm.** We propose a unified atom space in which all computations—encode, transfer, fuse, and reconstruct—are performed in the dictionary-coefficient representation, closing the loop beyond pixel space and keeping representations and constraints in the same domain to boost interpretability and robustness.
- **Controllable completion with a weak semantic prior.** We introduce a frozen language model as a lightweight semantic prior that acts only as channel- or atom-wise linear modulation in the coefficient domain, enabling a single, controllable correction for VIS \rightarrow IR transfer and reducing missed thermal cues without introducing pixel-level artifacts or instability.
- **Simple training and low-overhead inference.** Inference requires no real IR—only a visible image and the shared dictionary. Training uses reconstruction and simple consistency losses, avoiding adversarial or diffusion machin-

ery. The system maintains stability while remaining reproducible, deployable, and efficient.

2. Related Work

2.1. Typical IR-VIS Image Fusion

IR-VIS image fusion methods can be categorized into four groups based on their backbone architectures: CNN-based [8, 12, 16, 23, 24, 27], CNN-Transformer hybrid [15, 19, 22, 28, 34, 41], GAN-based [21, 32, 33, 36, 47, 53], and diffusion model-based [25, 40, 46, 48, 50] approaches.

CNN-based methods exploit the strength of convolution in local pattern modeling. Through multi-scale convolution, residual aggregation, and texture enhancement, they improve detail and contrast, as in SEDRFuse [12], ML-Fusion [16], and FusionNet [8]. These models are stable and lightweight but struggle to capture global dependencies, leading to inconsistent contrast or structural mismatch under complex illumination or cross-modal variation. CNN-Transformer hybrids, such as IVFWSR [19], CoCoNet [28] and SwinFusion [34] combine convolutional locality with Transformer-based global modeling. While achieving better dependency representation, they often suffer from high parameter scale, unstable training, and reduced inference efficiency. GAN-based methods enhance perceptual realism via adversarial learning. Dual- and attention-based discriminators, such as DDcGAN [33], SD-DGAN [53], and GAN-FM [47], impose multi-dimensional perceptual constraints, improving subjective quality but risking mode collapse and convergence instability. Diffusion model-based approaches enhance high-fidelity generation and cross-modal consistency by modeling the denoising process as a Markov chain. For instance, Diffusion [46] captures multi-channel input distributions to improve color and brightness fidelity, whereas DRMF [40] adopts multi-stage denoising for balanced structure-texture restoration. Although effective for complex content, these methods entail high sampling cost and slow convergence.

Existing methods assume that both modalities are available during training and inference, and learn end-to-end mappings within the pixel or feature domain. When the IR modality is missing, these black-box generative paradigms often fail to maintain physical consistency and controllability. To address these limitations, this paper proposes an interpretable fusion framework for scenarios where the infrared modality is unavailable.

2.2. Model-Driven Unfolding Networks

Model-driven unfolding transforms iterative optimization into a hierarchical framework based on the data-consistency \rightarrow prior pattern. It maps iterations of classical algorithms to network layers and replaces hand-tuned hyperparameters with learnable ones. Networks thus learn step sizes, thresh-

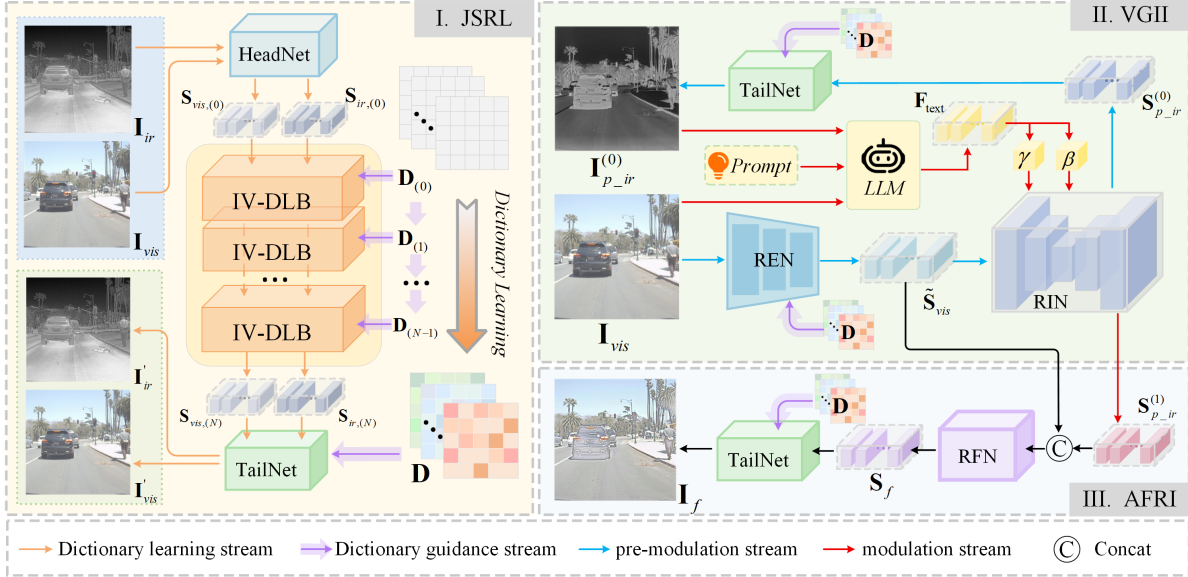


Figure 2. Architecture of the proposed framework. It integrates three modules (JSRL, VGII, and AFRI) to form a closed-loop pipeline of encoding, inference, fusion, and reconstruction. JSRL learns a shared dictionary for cross-modal alignment, VGII predicts latent infrared coefficients from visible ones, and AFRI fuses both modalities in the coefficient domain to reconstruct consistent, high-quality images under missing-IR conditions.

olds, and proximal operators in an end-to-end manner, enhancing interpretability and adaptability for complex tasks.

In dictionary learning and sparse coding, DKSVD [37] replaces the ℓ_0 prior with an ℓ_1 prior and unfolds sparse coding via ISTA [3] while parameterizing dictionaries with MLPs. Learned-CSC [5, 9, 10] integrates convolutional sparse coding with ISTA-based networks. Multi-scale feature extraction has been incorporated before ISTA unfolding for low-level vision tasks such as artifact removal. ADMM unfolding [4, 38] accelerates MRI reconstruction, while joint dictionaries with dual-branch LISTA unfolding enable multi-modal super-resolution. Proximal methods [1, 6] for convolutional sparse models with side information enhance multi-modal performance, and CNN-embedded iterative alignment improves MRI-CT registration. Proximal-gradient networks benefit multi-hyperspectral fusion, and learnable modality-aware units improve medical image segmentation accuracy.

This paradigm injects structured priors through explicit data consistency and learnable corrections, often outperforming black-box models under missing-modality or misalignment conditions. Building on this idea, we propose a unified convolutional dictionary framework that leverages the traditional IR-VIS fusion paradigm to enhance visible-image perception and improve downstream task performance when the infrared modality is missing.

3. Methodology

3.1. Overview

To address cross-modal incompleteness caused by the absence of the infrared image, we propose a correspondence prediction-based fusion framework grounded in dictionary learning. The core idea is to predict latent infrared representations from visible ones via a shared dictionary, enabling effective fusion under missing-modality conditions. As illustrated in Figure 2, the framework comprises three modules: JSRL, VGII, and AFRI. JSRL learns a shared dictionary that establishes structural correspondence between the two modalities. VGII exploits structural cues in visible coefficients to infer infrared coefficients through interpretable coefficient-domain prediction rather than direct generative reconstruction. AFRI fuses visible and inferred infrared coefficients and reconstructs the final image with the shared dictionary. Through their collaborative operation, the framework enhances perceptual quality and downstream task performance under missing-infrared conditions.

3.2. Joint Representation Learning

We propose JSRL to learn a cross-modal *shared dictionary* that represents visible and infrared images within a unified atom space. This shared representation provides a stable and interpretable foundation for subsequent visible-guided infrared inference and fusion. The objective jointly minimizes reconstruction errors of both modalities while impos-

ing coefficient priors and dictionary regularization:

$$\min_{\mathbf{D}, \mathbf{S}_{vis}, \mathbf{S}_{ir}} \frac{1}{2} \|\mathbf{I}_{vis} - \mathbf{D} * \mathbf{S}_{vis}\|_F^2 + \frac{1}{2} \|\mathbf{I}_{ir} - \mathbf{D} * \mathbf{S}_{ir}\|_F^2 + \lambda_1 \varphi_1(\mathbf{S}_{vis}) + \lambda_2 \varphi_2(\mathbf{S}_{ir}) + \lambda_3 \phi(\mathbf{D}). \quad (1)$$

Here, $*$ denotes convolution. $\mathbf{I}_{vis} \in \mathbb{R}^{m \times n}$ and $\mathbf{I}_{ir} \in \mathbb{R}^{m \times n}$ represent the visible and infrared images; $\mathbf{D} \in \mathbb{R}^{B \times k \times k}$ denotes the shared dictionary; and $\mathbf{S}_{vis} \in \mathbb{R}^{B \times m \times n}$ and $\mathbf{S}_{ir} \in \mathbb{R}^{B \times m \times n}$ denote the corresponding coefficient maps. $\varphi_1(\mathbf{S}_{vis})$ and $\varphi_2(\mathbf{S}_{ir})$ denote priors on the coefficients (typically a sparsity prior), and $\phi(\mathbf{D})$ denotes a dictionary regularization term, such as column-wise normalization and near-orthogonality. λ_1 , λ_2 and λ_3 are the balance parameters.

In objective (1), if $\varphi_1(\mathbf{S}_{vis})$, $\varphi_2(\mathbf{S}_{ir})$, and $\phi(\mathbf{D})$ are pre-defined, the dictionary \mathbf{D} and coefficients can be explicitly obtained through an optimization algorithm. However, manually defined priors and regularizations make the process complex and less generalizable to large-scale or diverse data. Inspired by [7, 52], we introduce deep subnetworks, CoeNet and DicNet, which autonomously learn the joint representations \mathbf{S}_{vis} and \mathbf{S}_{ir} as well as the dictionary \mathbf{D} from data. Built upon the theoretical foundation of objective (1), the network unifies dictionary learning and coefficient inference, embedding prior and regularization knowledge into trainable parameters. This design eliminates handcrafted constraints and enhances scalability and representation capability. To maintain consistency with the underlying optimization, the coefficient maps \mathbf{S}_{vis} and \mathbf{S}_{ir} output by CoeNet are designed to satisfy

$$\min_{\mathbf{S}_{vis}, \mathbf{S}_{ir}} \frac{1}{2} \|\mathbf{I}_{vis} - \mathbf{D} * \mathbf{S}_{vis}\|_F^2 + \frac{1}{2} \|\mathbf{I}_{ir} - \mathbf{D} * \mathbf{S}_{ir}\|_F^2 + \lambda_1 \varphi_1(\mathbf{S}_{vis}) + \lambda_2 \varphi_2(\mathbf{S}_{ir}), \quad (2)$$

Since $\varphi_1(\mathbf{S}_{vis})$ and $\varphi_2(\mathbf{S}_{ir})$ are implicit, CoeNet cannot be directly trained using objective (2). To address this, auxiliary variables \mathbf{S}'_{vis} and \mathbf{S}'_{ir} are introduced following the method in [52], which decomposes objective (2) into

$$\begin{aligned} \min_{\mathbf{S}_{vis}, \mathbf{S}'_{vis}} \frac{1}{2} \|\mathbf{I}_{vis} - \mathbf{D} * \mathbf{S}'_{vis}\|_F^2 + \frac{\mu_1}{2} \|\mathbf{S}_{vis} - \mathbf{S}'_{vis}\|_F^2 + \lambda_1 \varphi_1(\mathbf{S}_{vis}), \\ \min_{\mathbf{S}_{ir}, \mathbf{S}'_{ir}} \frac{1}{2} \|\mathbf{I}_{ir} - \mathbf{D} * \mathbf{S}'_{ir}\|_F^2 + \frac{\mu_2}{2} \|\mathbf{S}_{ir} - \mathbf{S}'_{ir}\|_F^2 + \lambda_2 \varphi_2(\mathbf{S}_{ir}), \end{aligned} \quad (3)$$

where \mathbf{S}'_{vis} and \mathbf{S}'_{ir} are updated in the *data-consistency step*:

$$\begin{aligned} \min_{\mathbf{S}'_{vis}} \frac{1}{2} \|\mathbf{I}_{vis} - \mathbf{D} * \mathbf{S}'_{vis}\|_F^2 + \frac{\mu_1}{2} \|\mathbf{S}_{vis} - \mathbf{S}'_{vis}\|_F^2, \\ \min_{\mathbf{S}'_{ir}} \frac{1}{2} \|\mathbf{I}_{ir} - \mathbf{D} * \mathbf{S}'_{ir}\|_F^2 + \frac{\mu_2}{2} \|\mathbf{S}_{ir} - \mathbf{S}'_{ir}\|_F^2. \end{aligned} \quad (4)$$

These subproblems can be solved in the Fourier domain, from which closed-form solutions can be derived using the Sherman–Morrison formula [2]. The coefficient maps \mathbf{S}_{vis}

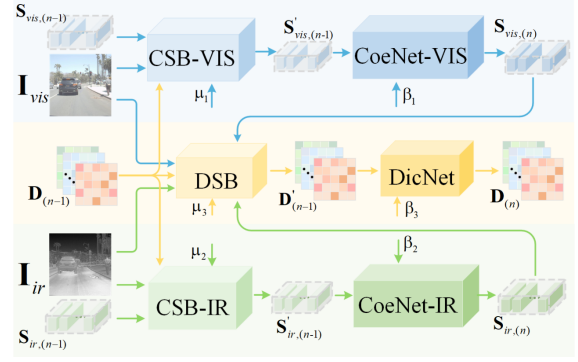


Figure 3. Structure of the IV-DLB.

and \mathbf{S}_{ir} are then updated via the following proximal sub-problems:

$$\begin{aligned} \min_{\mathbf{S}_{vis}} \frac{\beta_1}{2} \|\mathbf{S}_{vis} - \mathbf{S}'_{vis}\|_F^2 + \varphi_1(\mathbf{S}_{vis}), \\ \min_{\mathbf{S}_{ir}} \frac{\beta_2}{2} \|\mathbf{S}_{ir} - \mathbf{S}'_{ir}\|_F^2 + \varphi_2(\mathbf{S}_{ir}), \end{aligned} \quad (5)$$

These proximal updates can be expressed as:

$$\mathbf{S}_{vis} = \text{CoeNet}(\mathbf{S}'_{vis}, \beta_1), \quad \mathbf{S}_{ir} = \text{CoeNet}(\mathbf{S}'_{ir}, \beta_2), \quad (6)$$

where μ_1 , μ_2 , β_1 and β_2 are adaptive implicit hyperparameters predicted by the subnetwork *HypNet*. They dynamically control the update strength according to the input content and iteration stage, enabling learnable modulation of prior influence within the unfolding framework.

Similarly, an auxiliary variable \mathbf{D}' is introduced to formulate the dictionary learning problem as

$$\begin{aligned} \min_{\mathbf{D}, \mathbf{D}'} \frac{1}{2} \|\mathbf{I}_{vis} - \mathbf{D}' * \mathbf{S}_{vis}\|_F^2 + \frac{1}{2} \|\mathbf{I}_{ir} - \mathbf{D}' * \mathbf{S}_{ir}\|_F^2 \\ + \frac{\mu_3}{2} \|\mathbf{D} - \mathbf{D}'\|_F^2 + \lambda_3 \phi(\mathbf{D}), \end{aligned} \quad (7)$$

where \mathbf{D}' is updated in the *data-consistency step*:

$$\begin{aligned} \min_{\mathbf{D}'} \frac{1}{2} \|\mathbf{I}_{vis} - \mathbf{D}' * \mathbf{S}_{vis}\|_F^2 + \frac{1}{2} \|\mathbf{I}_{ir} - \mathbf{D}' * \mathbf{S}_{ir}\|_F^2 \\ + \frac{\mu_3}{2} \|\mathbf{D} - \mathbf{D}'\|_F^2, \end{aligned} \quad (8)$$

and \mathbf{D} is updated through a proximal mapping:

$$\arg \min_{\mathbf{D}} \frac{\beta_3}{2} \|\mathbf{D} - \mathbf{D}'\|_F^2 + \phi(\mathbf{D}). \quad (9)$$

This can be implemented using DicNet as follows:

$$\mathbf{D} = \text{DicNet}(\mathbf{D}', \beta_3). \quad (10)$$

where μ_3 and β_3 is also predicted by the *HypNet*.

To ensure consistency between the coefficient maps \mathbf{S}_{vis} , \mathbf{S}_{ir} predicted by CoeNet and the shared dictionary \mathbf{D} predicted by DicNet in satisfying Eqs. (5) and (9), the networks are first trained with reconstruction-based losses:

$$\begin{aligned} \ell_S = \|\mathbf{D}_{(n-1)} * \mathbf{S}_{vis,(n)} - \mathbf{I}_{vis}\|_1 + \|\mathbf{D}_{(n-1)} * \mathbf{S}_{ir,(n)} - \mathbf{I}_{ir}\|_1, \\ \ell_D = \|\mathbf{D}_{(n)} * \mathbf{S}_{vis,(n)} - \mathbf{I}_{vis}\|_1 + \|\mathbf{D}_{(n)} * \mathbf{S}_{ir,(n)} - \mathbf{I}_{ir}\|_1. \end{aligned} \quad (11)$$

where $n = 1, 2, \dots, N$ denotes the n -th update step.

As shown in Figure 2, the dictionary generation network consists of N cascaded Infrared–Visible Dictionary Learning Blocks (IV-DLBs), with a HeadNet for input decomposition and a TailNet for image reconstruction. The HeadNet includes two convolutional layers and a ReLU. As shown in Figure 3, Each IV-DLB contains two coefficient solvers and a dictionary solver. The coefficient solver comprises a Coefficient Solving Block (CSB) and a CoeNet. CSB performs frequency-domain orthogonalization to reduce atom correlation and improve conditioning, while CoeNet adopts a U-Net with symmetric residual encoder–decoder modules. The dictionary solver, consisting of a Dictionary Solving Block (DSB) and a DicNet. DSB updates kernels \mathbf{d} via proximal regularized least squares and solves all spatial positions in one pass using Cholesky decomposition. DicNet stacks three residual convolutional modules with ReLU activations. TailNet uses linear convolution with reflection padding to preserve boundaries. This architecture realizes the data-consistency (Eqs. (4), (8)) and proximal-update (Eqs. (5), (9)) steps, embedding the shared cross-modal dictionary and interpretable atom space into trainable components. Finally, *HypNet* takes the scale factor σ as input and predicts stage-wise hyperparameters using two 1×1 convolutions, followed by a Softplus activation to ensure positivity.

3.3. Visible-Guided Infrared Inference

In the previous section, a unified atom space based on the shared cross-modal dictionary is established. Unlike direct pixel-level generation, the modality transfer from visible to infrared is performed in the dictionary–coefficient domain, ensuring structural consistency and interpretability. Specifically, the visible image \mathbf{I}_{vis} is encoded by representation encode network (REN) as $\tilde{\mathbf{S}}_{vis} = \text{REN}(\mathbf{I}_{vis}; \mathbf{D}) \in \mathbb{R}^{B \times m \times n}$, where REN includes the pre-trained *HeadNet*, CSB-VIS, and CoeNet-VIS from JSRL. All REN parameters are frozen during coefficient generation to strictly follow the “data-consistency + proximal” principle in Eqs. (4), (5), preserving the physical interpretability of the shared dictionary \mathbf{D} and avoiding task-specific drift. This process projects visible information into the unified atom space, mitigating cross-modal inconsistencies common in pixel-domain learning. To infer the corresponding infrared coefficients, a Representation Inference Network (RIN) is introduced: $\mathbf{S}_{p-ir}^{(0)} = \text{RIN}(\tilde{\mathbf{S}}_{vis}) \in \mathbb{R}^{B \times m \times n}$. RIN employs an encoder–decoder architecture with attention-based down-sampling and up-sampling modules, each integrating multi-head attention for spatial and channel interaction. By operating in the coefficient domain rather than the pixel domain, RIN directly learns atom-level relationships within the shared dictionary, naturally inheriting the interpretability and structural coherence of JSRL.

A single transfer may fail to capture fine thermal cues in real infrared images, such as subtle temperature contrasts under low illumination. To refine these cues, a Large Language Model (LLM) is introduced as a semantic critic. The initial pseudo-infrared image is reconstructed via the shared dictionary and TailNet: $\mathbf{I}_{p-ir}^{(0)} = \text{TailNet}(\mathbf{S}_{p-ir}^{(0)}, \mathbf{D})$. The pair $\{\mathbf{I}_{vis}, \mathbf{I}_{p-ir}^{(0)}\}$ and a task description form a prompt fed into the frozen LLM to extract text features \mathbf{F}_{text} . Two multi-layer perceptrons then predict Feature-wise Linear Modulation parameters:

$$\gamma = \Phi_\gamma(\mathbf{F}_{text}), \quad \beta = \Phi_\beta(\mathbf{F}_{text}). \quad (12)$$

Semantic-guided affine modulation is applied in the coefficient domain to yield refined visible coefficients:

$$\mathbf{S}_{fm} = \gamma \odot \tilde{\mathbf{S}}_{vis} + \beta, \quad (13)$$

which are passed through RIN for the second-stage transfer and final reconstruction:

$$\mathbf{S}_{p-ir}^{(1)} = \text{RIN}(\mathbf{S}_{fm}), \quad \mathbf{I}_{p-ir} = \text{TailNet}(\mathbf{S}_{p-ir}^{(1)}, \mathbf{D}). \quad (14)$$

Rather than generating pixels or discriminating outputs, the LLM provides a weak semantic prior to modulate atomic responses in the coefficient space, enhancing thermal semantics without introducing generative noise. This closed-loop refinement operates entirely within the interpretable coefficient domain, complementing the shared dictionary to improve semantic completion under missing-modality conditions.

To ensure data consistency, thermal alignment, and structural fidelity, the total infrared inference loss is defined as

$$\ell_{inf} = \ell_{int} + \ell_{reg} + \ell_{grad}. \quad (15)$$

The consistency term constrains the pseudo-infrared image to match the real infrared in both image and coefficient domains:

$$\ell_{int} = \|\mathbf{I}_{p-ir} - \mathbf{I}_{ir}\|_1 + \|\mathbf{S}_{p-ir}^{(1)} - \mathbf{S}_{ir}\|_1. \quad (16)$$

Thermal regularization enforces intensity alignment using a normalized weighting map \mathbf{A}_{ir} :

$$\ell_{reg} = \|\mathbf{A}_{ir} \odot \mathbf{I}_{p-ir} - \mathbf{I}_{ir}\|_1, \quad \mathbf{A}_{ir} = \frac{\mathbf{I}_{ir} - \min(\mathbf{I}_{ir})}{\max(\mathbf{I}_{ir}) - \min(\mathbf{I}_{ir}) + \varepsilon} \quad (17)$$

where $\varepsilon = 10^{-8}$ avoids division by zero and \odot denotes element-wise multiplication. The gradient loss anchors geometric consistency by aligning image edges:

$$\ell_{grad} = \|\nabla \mathbf{I}_{p-ir} - \nabla \mathbf{I}_{vis}\|_1. \quad (18)$$

This design integrates coefficient-domain transfer, semantic modulation, and shared-dictionary reconstruction, extending the interpretable “data-consistency + proximal” paradigm of JSRL. By introducing a weak semantic prior, it achieves stable and reliable visible-guided infrared inference under missing-modality conditions.

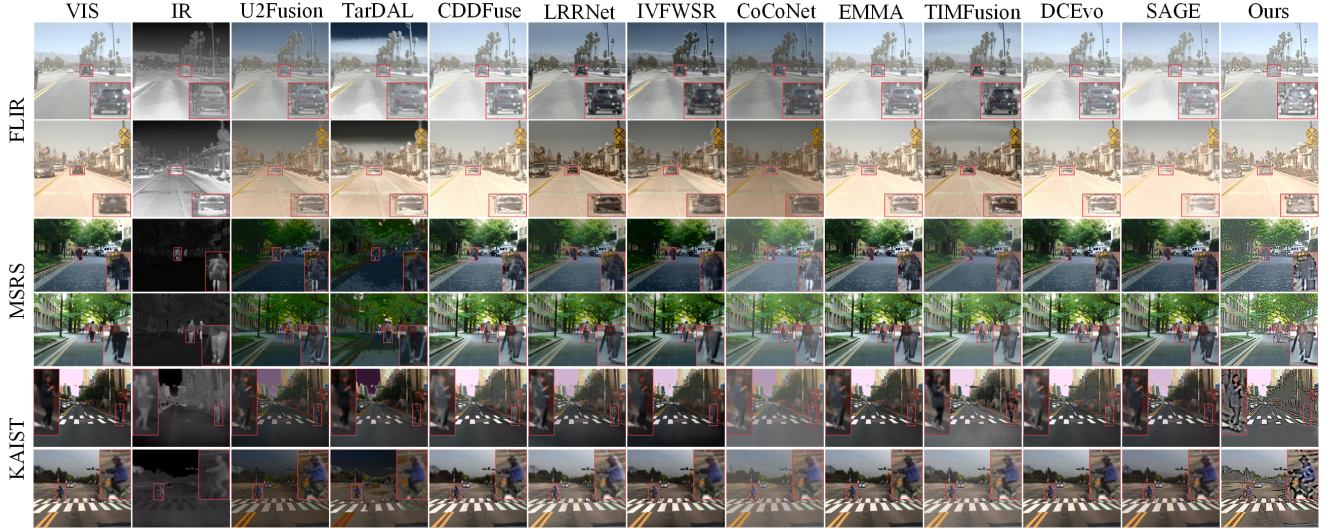


Figure 4. Visual comparison results on the FLIR, MSRS, and KAIST datasets for fused image quality.

3.4. Adaptive Fusion with Representation Inference

To adaptively integrate the structural information of the visible modality with the predicted infrared semantics in the coefficient domain, a Reasoning Fusion Network (RFN) is constructed. RFN consists of two cascaded Convolution–Attention Fusion (CAF) blocks, each combining window self-attention with convolutional mixing. The first block uses $\{\text{Conv}, \text{ReLU}, \text{Conv}, \text{ReLU}, \text{Conv}\}$, and the second $\{\text{Conv}, \text{ReLU}, \text{Conv}\}$, enabling local-to-global reasoning across atom and channel dimensions. Given the inputs $\tilde{\mathbf{S}}_{vis}$ and $\mathbf{S}_{p.ir}^{(1)}$, an implicit atom-wise gating mechanism $(\mathbf{W}_{vis}, \mathbf{W}_{p.ir}) = \Psi_{gate}(\text{Concat}(\tilde{\mathbf{S}}_{vis}, \mathbf{S}_{p.ir}^{(1)}))$ learns adaptive weights for each atom, producing the fused coefficients

$$\mathbf{S}_f = \mathbf{W}_{vis} \odot \tilde{\mathbf{S}}_{vis} + \mathbf{W}_{p.ir} \odot \mathbf{S}_{p.ir}^{(1)}, \quad (19)$$

where \odot denotes element-wise multiplication. This gating operates in the coefficient domain, allowing each dictionary atom to adaptively draw from visible or inferred infrared cues according to saliency. Atoms along structural edges favor $\tilde{\mathbf{S}}_{vis}$, while those encoding thermal semantics rely on $\mathbf{S}_{p.ir}^{(1)}$. Consequently, the framework achieves cross-modal collaboration within the unified atom space.

The fused coefficients, along with the shared dictionary \mathbf{D} are fed into TailNet, and the generated image is given by: $\mathbf{I}_f = \text{TailNet}(\mathbf{S}_f, \mathbf{D})$. Here, the reconstruction network and dictionary are consistent with those used in encoding and inference, forming a closed loop of “encoding \rightarrow inference \rightarrow fusion \rightarrow reconstruction.” This ensures that the fusion result lies within the interpretable subspace spanned by the shared atoms. To highlight thermal saliency while preserving visible structures, RFN is trained using intensity

and gradient consistency losses:

$$\begin{aligned} \ell_{int}^{fuse} &= \|\mathbf{I}_f - \max(\mathbf{I}_{p.ir}, \mathbf{I}_{vis})\|_1, \\ \ell_{grad}^{fuse} &= \|\nabla \mathbf{I}_f - \max(\nabla \mathbf{I}_{p.ir}, \nabla \mathbf{I}_{vis})\|_1. \end{aligned} \quad (20)$$

The element-wise “max” operation encourages \mathbf{I}_f to inherit thermal intensity peaks and sharp structural edges from infrared and visible inputs, respectively. The total fusion loss is then

$$\ell_f = \ell_{int}^{fuse} + \ell_{grad}^{fuse}. \quad (21)$$

4. Experiment

4.1. Experimental Setup

Datasets. We evaluate fusion performance on the FLIR, KAIST [11], and MSRS [39] datasets, and assess downstream performance, including object detection and semantic segmentation, on the M³FD [26] and FMB [27] datasets. Specifically, we randomly select 5,445 training pairs and 765 testing pairs from FLIR, 8,310 training pairs and 1,246 testing pairs from KAIST, and 536 training pairs and 179 testing pairs from MSRS. All images are randomly cropped into 128×128 patches.

Implementation Details. The JSRL, VGII and AFRI modules are trained sequentially. The JSRL module is trained on the MSRS for 1,000 epochs with a batch size of 24 and an initial learning rate of 0.0001. The dictionary trained by MSRS can be universally applied to other datasets in subsequent usage. The VGII and AFRI modules are trained for 10 epochs, both with a batch size of 10 and an initial learning rate of 0.001. The Adam optimizer [13] is used to update all parameters. In the JSRL module, the convolutional kernel size for the joint dictionary is set to 5×5 , and an IV-DLB is used. All experiments are conducted on

Table 1. Quantitative comparison of the fusion results of our method and existing methods on the MSRS, FLIR, and KAIST datasets. The best and second-best performances are highlighted with Red and Blue backgrounds, respectively.

Methods	MSRS						FLIR						KAIST					
	AG ↑	CE ↓	EI ↑	EN ↑	Qcb ↑	SF ↑	AG ↑	CE ↓	EI ↑	EN ↑	Qcb ↑	SF ↑	AG ↑	CE ↓	EI ↑	EN ↑	Qcb ↑	SF ↑
U2Fusion	2.308	0.840	24.692	6.145	0.483	6.288	4.645	1.353	48.215	6.916	0.410	11.302	3.262	1.626	34.797	6.092	0.505	9.399
TarDAL	2.189	2.183	23.251	6.059	0.417	6.379	3.722	0.643	39.761	7.393	0.420	9.392	1.815	1.273	19.393	6.282	0.431	5.355
CDDFuse	4.818	1.609	51.368	7.321	0.565	14.250	5.079	0.726	52.633	6.766	0.454	13.346	3.167	1.298	34.043	7.122	0.497	9.194
LRRNet	3.621	2.837	38.519	6.930	0.461	10.731	4.648	1.798	49.145	7.063	0.481	12.449	2.939	1.475	31.707	7.032	0.463	8.213
IVFWSR	3.360	1.337	36.254	6.798	0.457	9.241	3.386	1.266	36.392	7.365	0.400	8.144	2.672	0.868	28.868	6.959	0.443	7.743
CoCoNet	3.299	0.758	34.565	6.510	0.427	9.804	2.856	1.848	29.542	6.591	0.492	7.340	1.995	0.963	21.090	6.233	0.474	5.912
EMMA	4.913	1.343	52.642	7.333	0.539	14.176	3.796	0.745	40.356	6.489	0.451	10.188	3.083	0.859	33.405	7.005	0.514	8.837
TIMFusion	3.649	3.796	38.972	6.846	0.394	10.771	4.202	1.541	44.643	7.030	0.415	11.768	3.194	1.899	34.409	6.998	0.438	8.831
DCEvo	4.858	1.696	51.810	7.298	0.571	14.262	4.585	0.812	48.435	6.763	0.465	12.097	3.229	1.453	34.459	7.027	0.517	9.879
SAGE	4.452	2.058	47.134	7.030	0.529	13.285	3.254	0.697	33.860	6.646	0.376	9.115	2.950	1.037	31.467	6.799	0.520	8.835
Ours	5.037	3.142	53.168	7.188	0.454	14.898	4.518	0.596	48.784	6.639	0.435	12.554	4.414	2.227	37.115	7.073	0.405	11.031

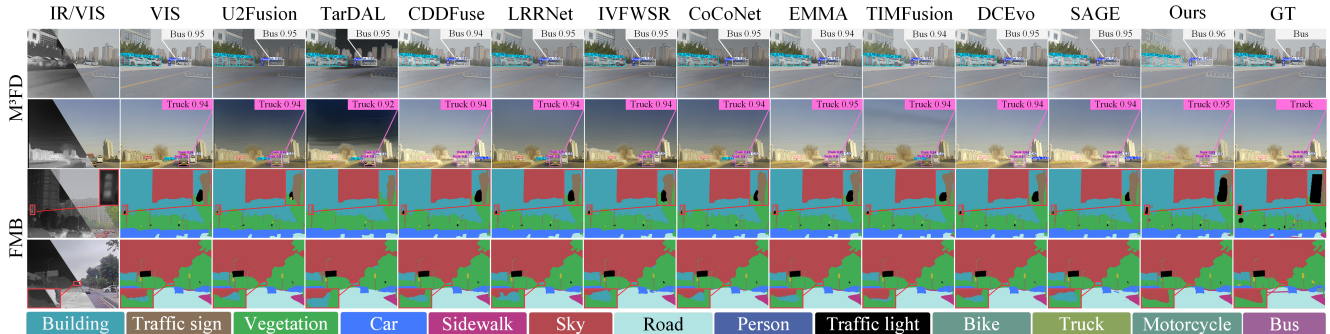


Figure 5. Qualitative comparison of object detection and semantic segmentation on the M³FD and FMB datasets, respectively.

two NVIDIA GeForce RTX 4090 GPUs, and the model is implemented using the PyTorch 3.10.18 framework.

4.2. Comparison with State-of-the-arts

To evaluate the effectiveness of our method, we compare it with ten state-of-the-art infrared and visible image fusion methods, including U2Fusion [44], TarDAL [26], CDDFuse [49], LRRNet [17], IVFWSR [20], CoCoNet [28], EMMA [51], TIMFusion [30], DCEvo [29], and SAGE [42]. In our experiments, the proposed method requires only visible images as input, whereas all comparison methods require both infrared and visible images.

Figure 4 presents the qualitative results of different methods. Our method shows superior detail fidelity, thermal information representation, brightness and contrast balance, and overall visual consistency. These observations indicate that, even without access to the infrared modality, our method can effectively recover infrared information. The quantitative comparisons are summarized in Table 1. The results show that our method achieves performance comparable to fusion approaches that take both infrared and visible images as input across all evaluation metrics. **It is worth noting that the supplementary material also includes comparisons with results obtained by fusing visible images with generated infrared images.**

4.3. Performance on Downstream Tasks

To further evaluate the effect of different methods on downstream tasks, we conduct object detection and semantic segmentation experiments on the M³FD and FMB datasets, respectively. The results are shown in Table 2 and Figure 5. For object detection, the fused images are used to train and test the YOLOv5s¹ model, while for semantic segmentation, they are used to train and test the SegFormer-b5 [43] model.

As shown in Table 2, our method exhibits performance comparable to that of full-modal fusion methods in terms of the mAP metric, with the AP values for most object categories reaching high levels. The visual results in Figure 5 further confirm that, even in the absence of the infrared modality, the detection model is able to accurately recognize and localize objects based on the images generated by our method. The detection confidence is consistent with that of the full-modal fusion images. Furthermore, as shown in Table 2, in the semantic segmentation task, the performance of our method is comparable to that of full-modal fusion methods, and in some metrics, it even outperforms them. The qualitative results in Figure 5 further illustrate that, compared to full-modal fusion methods, the images generated by our method are more accurately segmented into distinct semantic regions, with clearer boundaries and

¹<https://github.com/ultralytics/yolov5>

Table 2. Quantitative comparison of the object detection and semantic segmentation results of our method and existing methods on the M³FD and FMB datasets, respectively. Best results are highlighted in **red** and second-best in **blue**.

Methods	M ³ FD							FMB						
	people	car	bus	motor	truck	lamp	mAP	wall	building	sky	floor	tree	road	mIoU
VIS	0.864	0.964	0.990	0.926	0.908	0.970	0.931	89.461	58.723	85.666	33.918	67.091	95.984	61.794
U2Fusion	0.841	0.959	0.989	0.918	0.878	0.970	0.926	89.523	57.843	85.234	33.852	65.076	94.965	60.829
TarDAL	0.896	0.976	0.993	0.951	0.913	0.983	0.952	87.462	52.695	77.013	31.397	53.117	90.756	56.194
CDDFuse	0.883	0.974	0.991	0.943	0.903	0.976	0.945	89.811	57.901	87.383	32.988	67.748	96.055	61.649
LRRNet	0.898	0.978	0.993	0.958	0.904	0.986	0.953	89.705	59.081	86.685	34.596	66.974	95.678	62.942
IVFWSR	0.876	0.974	0.991	0.948	0.927	0.984	0.952	88.673	59.003	85.711	34.307	63.281	95.324	60.801
CoCoNet	0.893	0.974	0.991	0.947	0.899	0.982	0.948	89.630	57.803	86.597	32.492	64.982	95.653	58.513
EMMA	0.898	0.978	0.994	0.956	0.909	0.984	0.953	90.132	55.686	87.584	33.191	68.315	96.055	61.952
TIMFusion	0.896	0.977	0.993	0.958	0.913	0.984	0.954	89.911	56.663	87.015	32.953	66.018	95.874	62.836
DCEvo	0.885	0.975	0.989	0.946	0.907	0.977	0.946	89.372	56.562	87.231	33.876	68.513	96.075	60.366
SAGE	0.900	0.977	0.993	0.960	0.924	0.985	0.956	88.189	55.754	86.682	33.715	66.070	95.774	60.777
Ours	0.902	0.972	0.994	0.967	0.919	0.990	0.948	89.549	65.923	87.178	36.346	67.578	95.967	62.939

improved internal consistency. These findings strongly suggest that the high-quality images produced by our method offer enhanced adaptability for downstream tasks.

Table 3. Quantitative comparison between our model and its ablated variants. The best result for each metric is highlighted in **Red**.

Methods	Dictionary	LLM	AG \uparrow	CE \downarrow	EI \uparrow	EN \uparrow	Qcb \uparrow	SF \uparrow
Model I	\times	\times	3.320	1.452	45.531	6.058	0.396	9.238
Model II	\checkmark	\times	4.363	1.046	48.351	6.578	0.434	11.936
Model III	\times	\checkmark	4.256	0.619	48.154	6.423	0.418	11.175
Ours	\checkmark	\checkmark	4.518	0.596	48.784	6.639	0.435	12.554

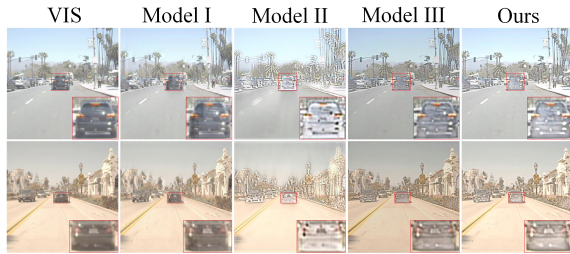


Figure 6. Qualitative comparison between our model and its ablated variants.

4.4. Ablation Study

The core of our method lies in the joint sparse dictionary and the LLM-based modulation. To evaluate the contribution of these two components to infrared and visible image fusion under the condition of missing infrared modality, we perform an ablation study on the FLIR dataset. The results are reported in Table 3 and Figure 6. We construct Model I as the baseline. In Model I, the joint dictionary is replaced with an encoder-decoder architecture that consists of three 3×3 convolutional layers, and the LLM-based modulation for infrared prediction is removed. As shown in Figure 6, Model I fails to recover infrared information and produces blurry results with noticeable artifacts compared to the source visible images.

Effectiveness of the Joint Sparse Dictionary. Building upon Model I, we replace the encoder and decoder structure composed of convolutional layers with a joint dictionary, resulting in Model II. The joint dictionary guides the process of image encoding and reconstruction. As shown in Figure 6, the introduction of the joint dictionary enables Model II to integrate infrared information into the generated images, thereby enhancing the thermal regions. The metrics in Table 3 further demonstrate improved image quality. These results indicate that the joint dictionary allows the model to more effectively capture cross modal correspondences in the joint representation space, facilitating better thermal compensation and fusion.

Effectiveness of LLM Modulation. Additionally, we integrate LLM guidance into Model I to provide discriminative supervision for infrared reasoning, resulting in Model III. As illustrated in Figure 6, the images generated by Model III display enhanced brightness and contrast, along with clearer edge details. The quantitative results in Table 3 further show that Model III outperforms Model I across all evaluation metrics. These findings imply that LLM effectively provides semantic constraints and discriminative cues during infrared reasoning, enabling the model to more accurately capture and preserve key thermal features.

In our full model, both the joint dictionary and LLM modulation are incorporated. As shown in Figure 6, the images generated by our model achieve the best visual performance, featuring superior detail preservation, texture quality, color fidelity, and enhancement of thermal regions. Moreover, as presented in Table 3, our method attains the highest scores across all evaluation metrics. These results underscore the complementary contributions of the joint dictionary and LLM modulation. **More experiments and analysis are provided in the supplementary material.**

5. Conclusion

We propose an IR-VIS fusion method tailored for scenarios where the infrared modality is absent. This method conducts coefficient domain fusion by imposing transfer and consistency constraints between visible coefficients and pseudo infrared coefficients within a shared dictionary space. The JSRL module establishes cross modal coefficient consistency. Under this consistency, the RIN performs interpretable reasoning for the missing modality and reconstructs thermal information from the visible representation. The AFRI module further enhances semantic consistent fusion and reconstruction by utilizing both visible and pseudo infrared representations, generating high quality images that preserve structural details and thermal cues. Experiments demonstrate that, despite the lack of infrared input, the proposed method achieves performance comparable to that of full modal fusion approaches. Moreover, it exhibits stable and superior performance in downstream tasks such as object detection and semantic segmentation.

Acknowledgments

This work was supported in part by the National Natural Science Foundation of China(62571222, 62276120, 62576163, 62161015), and the Yunnan Fundamental Research Projects (202501AS070123, 202301AV070004).

References

- [1] Jonas Adler and Ozan Öktem. Learned primal-dual reconstruction. *IEEE Transactions on Medical Imaging*, 37(6):1322–1332, 2018. 3
- [2] Mehmet A Akgün, John H Garcelon, and Raphael T Haftka. Fast exact linear and non-linear structural reanalysis and the sherman–morrison–woodbury formulas. *International Journal for Numerical Methods in Engineering*, 50(7):1587–1606, 2001. 4
- [3] Amir Beck and Marc Teboulle. A fast iterative shrinkage-thresholding algorithm for linear inverse problems. *SIAM Journal on Imaging Sciences*, 2(1):183–202, 2009. 3
- [4] Stephen Boyd, Neal Parikh, Eric Chu, Borja Peleato, Jonathan Eckstein, et al. Distributed optimization and statistical learning via the alternating direction method of multipliers. *Foundations and Trends in Machine learning*, 3(1):1–122, 2011. 3
- [5] Hilton Bristow, Anders Eriksson, and Simon Lucey. Fast convolutional sparse coding. In *Proceedings of the IEEE Conference on Computer Vision and Pattern Recognition*, pages 391–398, 2013. 3
- [6] Antonin Chambolle and Thomas Pock. A first-order primal-dual algorithm for convex problems with applications to imaging. *Journal of Mathematical Imaging and Vision*, 40(1):120–145, 2011. 3
- [7] Xin Deng, Jingyi Xu, Fangyuan Gao, Xiancheng Sun, and Mai Xu. Deep M²cdl: Deep multi-scale multi-modal convolutional dictionary learning network. *IEEE Transactions on Pattern Analysis and Machine Intelligence*, 46(5):2770–2787, 2023. 4
- [8] Keying Du, Huafeng Li, Yafei Zhang, and Zhengtao Yu. Chitnet: A complementary to harmonious information transfer network for infrared and visible image fusion. *IEEE Transactions on Instrumentation and Measurement*, 74:1–17, 2025. 2
- [9] Xueyang Fu, Zheng-Jun Zha, Feng Wu, Xinghao Ding, and John Paisley. Jpeg artifacts reduction via deep convolutional sparse coding. In *Proceedings of the IEEE/CVF International Conference on Computer Vision*, pages 2501–2510, 2019. 3
- [10] Shuhang Gu, Wangmeng Zuo, Qi Xie, Deyu Meng, Xi-angchu Feng, and Lei Zhang. Convolutional sparse coding for image super-resolution. In *Proceedings of the IEEE International Conference on Computer Vision*, pages 1823–1831, 2015. 3
- [11] Soonmin Hwang, Jaesik Park, Namil Kim, Yukyung Choi, and In So Kweon. Multispectral pedestrian detection: Benchmark dataset and baseline. In *Proceedings of the IEEE Conference on Computer Vision and Pattern Recognition*, pages 1037–1045, 2015. 6
- [12] Lihua Jian, Xiaomin Yang, Zheng Liu, Gwanggil Jeon, Mingliang Gao, and David Chisholm. Sedrfuse: A symmetric encoder–decoder with residual block network for infrared and visible image fusion. *IEEE Transactions on Instrumentation and Measurement*, 70:1–15, 2020. 2
- [13] Diederik P. Kingma and Jimmy Lei Ba. Adam: A method for stochastic optimization. In *International Conference on Learning Representations (ICLR)*, pages 1–15, 2015. 6
- [14] Dong-Guw Lee, Myung-Hwan Jeon, Younggun Cho, and Ayoung Kim. Edge-guided multi-domain rgb-to-tir image translation for training vision tasks with challenging labels. *arXiv preprint arXiv:2301.12689*, 2023. 2
- [15] Hui Li and Xiao-Jun Wu. Crossfuse: A novel cross attention mechanism based infrared and visible image fusion approach. *Information Fusion*, 103:102147, 2024. 2
- [16] Huafeng Li, Yueliang Cen, Yu Liu, Xun Chen, and Zhengtao Yu. Different input resolutions and arbitrary output resolution: A meta learning-based deep framework for infrared and visible image fusion. *IEEE Transactions on Image Processing*, 30:4070–4083, 2021. 2
- [17] Hui Li, Tianyang Xu, Xiao-Jun Wu, Jiwen Lu, and Josef Kittler. Lrrnet: A novel representation learning guided fusion network for infrared and visible images. *IEEE Transactions on Pattern Analysis and Machine Intelligence*, 45(9):11040–11052, 2023. 7
- [18] Huafeng Li, Junzhi Zhao, Jinxing Li, Zhengtao Yu, and Guangming Lu. Feature dynamic alignment and refinement for infrared–visible image fusion: Translation robust fusion. *Information Fusion*, 95:26–41, 2023. 1
- [19] Huafeng Li, Junyu Liu, Yafei Zhang, and Yu Liu. A deep learning framework for infrared and visible image fusion without strict registration. *International Journal of Computer Vision*, 132:1625–1644, 2024. 1, 2
- [20] Huafeng Li, Zengyi Yang, Yafei Zhang, Wei Jia, Zhengtao Yu, and Yu Liu. Mulfs-cap: Multimodal fusion-

- supervised cross-modality alignment perception for unregistered infrared-visible image fusion. *IEEE Transactions on Pattern Analysis and Machine Intelligence*, 47(5):3673–3690, 2025. 1, 7
- [21] Jing Li, Hongtao Huo, Chang Li, Renhua Wang, and Qi Feng. Attentionfgan: Infrared and visible image fusion using attention-based generative adversarial networks. *IEEE Transactions on Multimedia*, 23:1383–1396, 2020. 1, 2
- [22] Jing Li, Jianming Zhu, Chang Li, Xun Chen, and Bin Yang. Cgtf: Convolution-guided transformer for infrared and visible image fusion. *IEEE Transactions on Instrumentation and Measurement*, 71:1–14, 2022. 2
- [23] Xingyuan Li, Yang Zou, Jinyuan Liu, Zhiying Jiang, Long Ma, Xin Fan, and Risheng Liu. From text to pixels: A context-aware semantic synergy solution for infrared and visible image fusion. *arXiv preprint arXiv:2401.00421*, 2023. 2
- [24] Xingyuan Li, Jinyuan Liu, Zhixin Chen, Yang Zou, Long Ma, Xin Fan, and Risheng Liu. Contourlet residual for prompt learning enhanced infrared image super-resolution. In *European Conference on Computer Vision*, pages 270–288. Springer, 2024. 2
- [25] Xingyuan Li, Zirui Wang, Yang Zou, Zhixin Chen, Jun Ma, Zhiying Jiang, Long Ma, and Jinyuan Liu. Difiisr: A diffusion model with gradient guidance for infrared image super-resolution. In *Proceedings of the Computer Vision and Pattern Recognition Conference*, pages 7534–7544, 2025. 2
- [26] Jinyuan Liu, Xin Fan, Zhanbo Huang, Guanyao Wu, Risheng Liu, Wei Zhong, and Zhongxuan Luo. Target-aware dual adversarial learning and a multi-scenario multi-modality benchmark to fuse infrared and visible for object detection. In *Proceedings of the IEEE/CVF Conference on Computer Vision and Pattern Recognition*, pages 5802–5811, 2022. 6, 7
- [27] Jinyuan Liu, Zhu Liu, Guanyao Wu, Long Ma, Risheng Liu, Wei Zhong, Zhongxuan Luo, and Xin Fan. Multi-interactive feature learning and a full-time multi-modality benchmark for image fusion and segmentation. In *Proceedings of the IEEE/CVF international conference on computer vision*, pages 8115–8124, 2023. 2, 6
- [28] Jinyuan Liu, Runjia Lin, Guanyao Wu, Risheng Liu, Zhongxuan Luo, and Xin Fan. Coconet: Coupled contrastive learning network with multi-level feature ensemble for multi-modality image fusion. *International Journal of Computer Vision*, 132(5):1748–1775, 2024. 2, 7
- [29] Jinyuan Liu, Bowei Zhang, Qingyun Mei, Xingyuan Li, Yang Zou, Zhiying Jiang, Long Ma, Risheng Liu, and Xin Fan. Dcevo: Discriminative cross-dimensional evolutionary learning for infrared and visible image fusion. In *Proceedings of the Computer Vision and Pattern Recognition Conference*, pages 2226–2235, 2025. 7
- [30] Risheng Liu, Zhu Liu, Jinyuan Liu, Xin Fan, and Zhongxuan Luo. A task-guided, implicitly-searched and meta-initialized deep model for image fusion. *IEEE Transactions on Pattern Analysis and Machine Intelligence*, 46(10):6594–6609, 2024. 7
- [31] Yu Liu, Lei Wang, Huafeng Li, and Xun Chen. Multi-focus image fusion with deep residual learning and focus property detection. *Information Fusion*, 86:1–16, 2022. 1
- [32] Jiayi Ma, Wei Yu, Pengwei Liang, Chang Li, and Junjun Jiang. Fusiongan: A generative adversarial network for infrared and visible image fusion. *Information Fusion*, 48:11–26, 2019. 1, 2
- [33] Jiayi Ma, Han Xu, Junjun Jiang, Xiaoguang Mei, and Xiaoping Zhang. Ddcgan: A dual-discriminator conditional generative adversarial network for multi-resolution image fusion. *IEEE Transactions on Image Processing*, 29:4980–4995, 2020. 2
- [34] Jiayi Ma, Linfeng Tang, Fan Fan, Jun Huang, Xiaoguang Mei, and Yong Ma. Swinfusion: Cross-domain long-range learning for general image fusion via swin transformer. *IEEE/CAA Journal of Automatica Sinica*, 9(7):1200–1217, 2022. 1, 2
- [35] Fangyuan Mao, Jilin Mei, Shun Lu, Fuyang Liu, Liang Chen, Fangzhou Zhao, and Yu Hu. Pid: physics-informed diffusion model for infrared image generation. *Pattern Recognition*, page 111816, 2025. 2
- [36] Dongyu Rao, Tianyang Xu, and Xiao-Jun Wu. Tgfuse: An infrared and visible image fusion approach based on transformer and generative adversarial network. *IEEE Transactions on Image Processing*, 2023. 2
- [37] Meyer Scetbon, Michael Elad, and Peyman Milanfar. Deep k-svd denoising. *IEEE Transactions on Image Processing*, 30:5944–5955, 2021. 3
- [38] Jian Sun, Huibin Li, Zongben Xu, et al. Deep admm-net for compressive sensing mri. *Advances in Neural Information Processing Systems*, 29, 2016. 3
- [39] Linfeng Tang, Jiteng Yuan, Hao Zhang, Xingyu Jiang, and Jiayi Ma. Piafusion: A progressive infrared and visible image fusion network based on illumination aware. *Information Fusion*, 83:79–92, 2022. 6
- [40] Linfeng Tang, Yuxin Deng, Xunpeng Yi, Qinglong Yan, Yixuan Yuan, and Jiayi Ma. Drmf: Degradation-robust multi-modal image fusion via composable diffusion prior. In *Proceedings of the 32nd ACM International Conference on Multimedia*, pages 8546–8555, 2024. 2
- [41] Wei Tang, Fazhi He, Yu Liu, Yansong Duan, and Tongzhen Si. Datfuse: Infrared and visible image fusion via dual attention transformer. *IEEE Transactions on Circuits and Systems for Video Technology*, 33(7):3159–3172, 2023. 2
- [42] Guanyao Wu, Haoyu Liu, Hongming Fu, Yichuan Peng, Jinyuan Liu, Xin Fan, and Risheng Liu. Every sam drop counts: Embracing semantic priors for multi-modality image fusion and beyond. In *Proceedings of the Computer Vision and Pattern Recognition Conference*, pages 17882–17891, 2025. 7
- [43] Enze Xie, Wenhai Wang, Zhiding Yu, Anima Anandkumar, Jose M Alvarez, and Ping Luo. Segformer: Simple and efficient design for semantic segmentation with transformers. *Advances in Neural Information Processing Systems*, 34:12077–12090, 2021. 7
- [44] Han Xu, Jiayi Ma, Junjun Jiang, Xiaojie Guo, and Haibin Ling. U2fusion: A unified unsupervised image fusion network. *IEEE Transactions on Pattern Analysis and Machine Intelligence*, 44(1):502–518, 2020. 7

- [45] Zengyi Yang, Yafei Zhang, Huafeng Li, and Yu Liu. Instruction-driven fusion of infrared–visible images: Tailoring for diverse downstream tasks. *Information Fusion*, 121: 103148, 2025. [1](#)
- [46] Jun Yue, Leyuan Fang, Shaobo Xia, Yue Deng, and Jiayi Ma. Dif-fusion: Toward high color fidelity in infrared and visible image fusion with diffusion models. *IEEE Transactions on Image Processing*, 32:5705–5720, 2023. [2](#)
- [47] Hao Zhang, Jiteng Yuan, Xin Tian, and Jiayi Ma. Gan-fm: Infrared and visible image fusion using gan with full-scale skip connection and dual markovian discriminators. *IEEE Transactions on Computational Imaging*, 7:1134–1147, 2021. [2](#)
- [48] Hao Zhang, Lei Cao, and Jiayi Ma. Text-difuse: An interactive multi-modal image fusion framework based on text-modulated diffusion model. *Advances in Neural Information Processing Systems*, 37:39552–39572, 2024. [1](#), [2](#)
- [49] Zixiang Zhao, Haowen Bai, Jianshe Zhang, Yulun Zhang, Shuang Xu, Zudi Lin, Radu Timofte, and Luc Van Gool. Cddfuse: Correlation-driven dual-branch feature decomposition for multi-modality image fusion. In *Proceedings of the IEEE/CVF Conference on Computer Vision and Pattern Recognition*, pages 5906–5916, 2023. [7](#)
- [50] Zixiang Zhao, Haowen Bai, Yuanzhi Zhu, Jianshe Zhang, Shuang Xu, Yulun Zhang, Kai Zhang, Deyu Meng, Radu Timofte, and Luc Van Gool. Ddfm: denoising diffusion model for multi-modality image fusion. In *Proceedings of the IEEE/CVF International Conference on Computer Vision*, pages 8082–8093, 2023. [1](#), [2](#)
- [51] Zixiang Zhao, Haowen Bai, Jianshe Zhang, Yulun Zhang, Kai Zhang, Shuang Xu, Dongdong Chen, Radu Timofte, and Luc Van Gool. Equivariant multi-modality image fusion. In *Proceedings of the IEEE/CVF Conference on Computer Vision and Pattern Recognition*, pages 25912–25921, 2024. [7](#)
- [52] Hongyi Zheng, Hongwei Yong, and Lei Zhang. Deep convolutional dictionary learning for image denoising. In *Proceedings of the IEEE/CVF Conference on Computer Vision and Pattern Recognition*, pages 630–641, 2021. [4](#)
- [53] Huabing Zhou, Wei Wu, Yanduo Zhang, Jiayi Ma, and Haibin Ling. Semantic-supervised infrared and visible image fusion via a dual-discriminator generative adversarial network. *IEEE Transactions on Multimedia*, 25:635–648, 2021. [2](#)

Missing No More: Dictionary-Guided Cross-Modal Image Fusion under Missing Infrared

Supplementary Material

A. More Detail of Our Method

We present the process of Joint Shared-dictionary Representation Learning (JSRL) in Algorithm 1. First, the infrared and visible images are fed into the HeadNet to generate their coefficient maps, with the shared dictionary being initialized to zeros. Subsequently, these initial representations are progressively refined through N IV-DLBs, enabling the final coefficients and shared dictionary to accurately reconstruct the input infrared and visible images.

Algorithm 1 Joint Shared-dictionary Representation Learning

Input: Infrared image \mathbf{I}_{ir} , visible image \mathbf{I}_{vis} , scale factor σ , the number of IV-DLBs N

Output: Reconstructed infrared image \mathbf{I}'_{ir} , Reconstructed visible image \mathbf{I}'_{vis} , shared dictionary \mathbf{D}

- 1: $\mathbf{S}_{vis,(0)} = \text{HeadNet}(\mathbf{I}_{vis})$, $\mathbf{S}_{ir,(0)} = \text{HeadNet}(\mathbf{I}_{ir})$, $\mathbf{D}_{(0)} = \mathbf{0}$
- 2: **for** $n = 1$ to N **do**
- 3: $\{\mu_{1,(n)}, \mu_{2,(n)}, \mu_{3,(n)}, \beta_{1,(n)}, \beta_{2,(n)}, \beta_{3,(n)}\} = \text{HypNet}(\sigma)$
- 4: $\mathbf{S}'_{vis,(n)} = \text{CSB-VIS}(\mathbf{I}_{vis}, \mathbf{D}_{(n-1)}, \mathbf{S}_{vis,(n-1)}, \mu_{1,(n)})$
- 5: $\mathbf{S}_{vis,(n)} = \text{CoeNet-VIS}(\mathbf{S}'_{vis,(n)}, \beta_{1,(n)})$
- 6: $\mathbf{S}'_{ir,(n)} = \text{CSB-IR}(\mathbf{I}_{ir}, \mathbf{D}_{(n-1)}, \mathbf{S}_{ir,(n-1)}, \mu_{2,(n)})$
- 7: $\mathbf{S}_{ir,(n)} = \text{CoeNet-IR}(\mathbf{S}'_{ir,(n)}, \beta_{2,(n)})$
- 8: $\mathbf{D}'_{(n)} = \text{DSB}(\mathbf{I}_{vis}, \mathbf{I}_{ir}, \mathbf{D}_{(n-1)}, \mathbf{S}_{vis,(n)}, \mathbf{S}_{ir,(n)}, \mu_{3,(n)})$
- 9: $\mathbf{D}_{(n)} = \text{DicNet}(\mathbf{D}'_{(n)}, \beta_{3,(n)})$
- 10: **end for**
- 11: $\mathbf{I}'_{vis} = \mathbf{D}_{(N)} * \mathbf{S}_{vis,(N)}$, $\mathbf{I}'_{ir} = \mathbf{D}_{(N)} * \mathbf{S}_{ir,(N)}$

In addition, we summarize the training pipeline for the VIS-Guided IR Inference (VGII) and Adaptive Fusion via Representation Inference (AFRI) modules in Algorithm 2.

B. Hyperparameter Analysis

The proposed method involves two key hyperparameters: the kernel size of the dictionary and the number of IV-DLBs. In our implementation, we set the kernel size of the dictionary to 5×5 and use a single IV-DLB layer. In this section, we analyze the influence of the hyperparameters on model performance on the FLIR dataset.

Influence of the dictionary kernel size. To evaluate the impact of the dictionary kernel size on model performance, we evaluate three different kernel configurations: 3×3 , 5×5 , and 7×7 . As shown in Table 4, increasing the kernel size from 3×3 to 5×5 results in notable improvements across all metrics. However, further enlarging the kernel to 7×7

Algorithm 2 VIS-Guided IR Inference and Adaptive Fusion via Representation Inference

Input: visible image \mathbf{I}_{vis} , shared dictionary \mathbf{D} , pretrained LLM: Qwen-7B-Chat

Output: Fusion image \mathbf{I}_f

- 1: $\tilde{\mathbf{S}}_{vis} = \text{REN}(\mathbf{I}_{vis}, \mathbf{D})$
- 2: $\mathbf{S}_{p.ir}^{(0)} = \text{RIN}(\tilde{\mathbf{S}}_{vis})$
- 3: $\mathbf{I}_{p.ir}^{(0)} = \text{TailNet}(\mathbf{S}_{p.ir}^{(0)}, \mathbf{D})$
- 4: $\mathbf{F}_{text} = \text{LLM}(\mathbf{I}_{vis}, \mathbf{I}_{p.ir}^{(0)})$
- 5: $\gamma = \Phi_\gamma(\mathbf{F}_{text})$, $\beta = \Phi_\beta(\mathbf{F}_{text})$
- 6: $\mathbf{S}_{p.ir}^{(1)} = \text{RIN}(\gamma \odot \tilde{\mathbf{S}}_{vis} + \beta)$
- 7: $\{\mathbf{W}_{vis}, \mathbf{W}_{p.ir}\} = \Psi_{gate}(\text{Concat}(\tilde{\mathbf{S}}_{vis}, \mathbf{S}_{p.ir}^{(1)}))$
- 8: $\mathbf{I}_f = \text{TailNet}(\mathbf{W}_{vis}, \tilde{\mathbf{S}}_{vis}, \mathbf{W}_{p.ir}, \mathbf{S}_{p.ir}^{(1)})$

Table 4. Influence of the dictionary kernel size on model performance. The best performance for each metric is marked with Red .

Kernel size	AG \uparrow	CE \downarrow	EI \uparrow	EN \uparrow	Qcb \uparrow	SF \uparrow
3×3	4.156	1.357	44.882	6.545	0.430	11.195
5×5	4.518	0.596	48.784	6.639	0.435	12.554
7×7	4.499	1.298	48.560	6.627	0.356	12.300

leads to varying degrees of performance degradation. 5×5 yields the best overall fusion performance.

Influence of the number of IV-DLB. To evaluate the effect of the number of IV-DLBs, we conduct experiments with $N = 1, 2, 3$. As shown in Table 5, increasing N from 1 to 2 leads to only marginal performance gains, while the FLOPs nearly doubles. Further increasing N to 3 results in a degradation of performance. Therefore, we introduce an IV-DLB layer in our experiments to achieve a favorable trade-off between model performance and computational complexity.

Table 5. Influence of the number of IV-DLBs on model performance. The best performance for each metric is marked with Red .

N	AG \uparrow	CE \downarrow	EI \uparrow	EN \uparrow	Qcb \uparrow	SF \uparrow	GFLOPS
1	4.518	0.596	48.784	6.639	0.435	12.554	63.023
2	4.529	0.565	49.096	6.598	0.432	12.671	120.795
3	4.485	0.679	48.641	6.705	0.432	12.265	178.567

Influence of the textual prompt. To evaluate the impact

of textual prompt from LLM on the model performance, we conducted experiments by setting up three different types of text prompts. As shown in the Table 6, the experiment proved that the change in cues had an impact on the effect of fusion. The simplified prompts used in this experiment and the contrast experiment are shown in the Figure 7 below. Among them, our prompts achieved the best performance.

Table 6. Influence of the textual prompt on model performance. The best performance for each metric is marked with Red .

Prompt	AG \uparrow	CE \downarrow	EI \uparrow	EN \uparrow	Qcb \uparrow	SF \uparrow
No Prompt	4.183	1.016	47.166	6.215	0.401	11.694
Simplified Prompt	4.431	0.610	48.687	6.613	0.419	12.186
Complete Prompt	4.518	0.596	48.784	6.639	0.435	12.554

This is a synthetic infrared image generated from the visible image. Please analyze how realistic this infrared image appears, and suggest what modifications are needed to make it more physically accurate. Focus on thermal distribution, contrast, and texture fidelity.

This is a synthetic infrared image generated from a visible image. Please evaluate its realism and suggest improvements.

(a)Static textual prompt

(b)Simplified prompt

Figure 7. Two different types of text prompts. A is the complete prompt used in the experiment, while B is the simplified version of the prompt.

C. Evaluation Metrics

Since there is no existing metric that can prove the absolute excellence of the fused image, we employed six widely recognized image fusion evaluation metrics to objectively assess the quality of the fusion results. Among them, the average gradient (AG) measures the edge intensity of the image, indicating that the fused image can effectively restore the boundary of the target object; The contrast entropy (CE) measures the distribution of contrast in an image; the edge intensity (EI) measures the clarity and strength of edges in the image; the image entropy (EN) measures the complexity of details in the image. A higher image entropy indicates that the image contains more information and has more variations; the quality consistency based on fusion (Q_{cb}) measures the quality consistency between the fused image and the reference image; the spatial frequency (SF) measures the spatial frequency of the image to ensure a better visual effect and clearer details in the fused image.

D. Complexity Analysis

In this section, we conduct a complexity analysis of the proposed method and compare it with several infrared-visible fusion methods that rely on infrared image generation. Table 7 presents the complexity comparison results and inference time for each image among different methods. Compared with other pixel-level generation fusion methods, our method shows a significantly lower number of learnable parameters, moderate FLOPs and inference time, while maintaining superior performance. This advantage stems from our feature-level infrared modal inference and fusion framework, which eliminates the need for generating infrared images, thereby reducing computational complexity.

Table 7. Complexity analysis of fusion models with missing infrared modality. All parameters listed in the table represent the learnable parameters of the models. The FLOPs and inference time for each model are calculated using input images of size 256×256 . 'E' denotes the EGGAN method, while 'P' denotes the PID method.

Model	Param (M)	FLOPs (G)	Time (s)	Qcb \uparrow
E+U2Fusion	48.064	710.385	0.103	0.368
E+TarDAL	46.892	96.768	0.052	0.304
E+CDDFuse	47.784	194.176	0.059	0.429
E+LRRNet	46.644	80.347	0.026	0.390
E+IVFSWR	60.098	936.753	0.176	0.422
E+CoCoNet	55.709	118.866	0.075	0.409
E+EMMA	48.111	85.935	0.038	0.427
E+TIMFusion	47.827	111.154	0.053	0.396
E+DCEvo	48.601	272.027	0.059	0.432
E+SAGE	46.731	212.942	0.062	0.403
<hr/>				
P+U2Fusion	242.895	2,921.78	11.066	0.388
P+TarDAL	241.723	2,308.16	11.015	0.282
P+CDDFuse	242.614	2,405.57	11.022	0.403
P+LRRNet	241.475	2,291.74	10.989	0.408
P+IVFSWR	254.929	3,148.14	11.139	0.377
P+CoCoNet	250.541	2,330.26	11.038	0.433
P+EMMA	242.776	2,297.33	11.002	0.390
P+TIMFusion	242.658	2,322.54	11.026	0.404
P+DCEvo	243.431	2,483.42	11.032	0.412
P+SAGE	241.562	2,424.33	11.025	0.339
<hr/>				
Ours	21.798	542.001	5.793	0.435

E. More experimental results

To further evaluate the performance of our method, we conduct additional comparative experiments under missing-IR modality. Specifically, we first employ pixel-level infrared generation methods to reconstruct the missing infrared images and then fused the generated infrared images with visible images. The selected infrared generation methods include PID [35], a GAN-based approach EGGAN [14], and a diffusion-based approach. The fusion process still adopts the ten mainstream fusion methods used in the main paper.

Our method does not generate infrared images. Instead, it directly infers infrared features from the input visible images and produces enhanced images through the adaptive fusion of infrared and visible features.

As illustrated in Figures 8 and 9, the qualitative results show that our method achieves an optimal balance among detail fidelity, thermal-target enhancement, and overall visual naturalness. The proposed approach effectively preserves the thermal information while fully integrating the structural and textural features of the visible image. In contrast, methods based on infrared generation suffer from modality imbalance, and their fusion results exhibit issues such as blurring, ghosting, and excessively bright or dark regions. The quantitative results in Tables 8 and 9 further validate that our method delivers superior performance across all evaluation metrics. These results clearly confirm that, for infrared-visible image fusion under missing infrared modality, our approach achieves state-of-the-art performance.

F. Limitations and Future Work

Although the proposed method is effective, it still has certain limitations. The method primarily addresses the catastrophic effects of missing infrared images but cannot fully replace the role of infrared images in challenging imaging environments. For example, under extreme weather conditions such as heavy fog, visible light imaging devices often fail to capture key targets, making it difficult to reliably infer significant infrared information from the visible images. This limitation constrains the upper bound of the fusion framework. In future work, we will further investigate fusion paradigms under missing infrared conditions, with a focus on enhancing the visual representation of visible images in uncontrollable imaging environments and reducing the uncertainty introduced by variations in imaging conditions and infrared feature inference. Additionally, we plan to incorporate more robust priors and learnable constraints to improve the method's generalization and stability in complex scenarios.

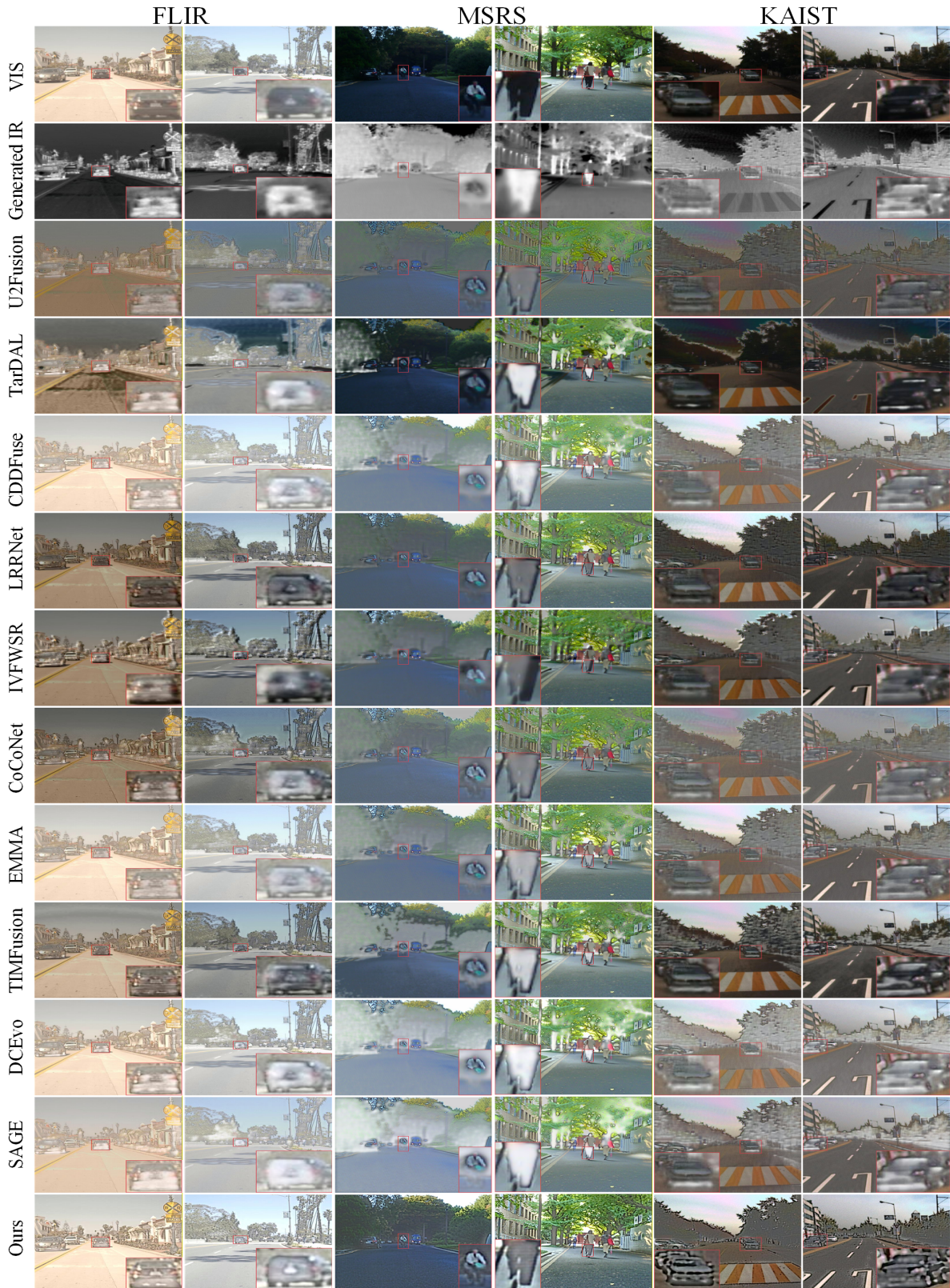


Figure 8. Visual comparison of different fusion methods on the FLIR, MSRS, and KAIST datasets, where the infrared images are generated from visible images using the EGGAN method.

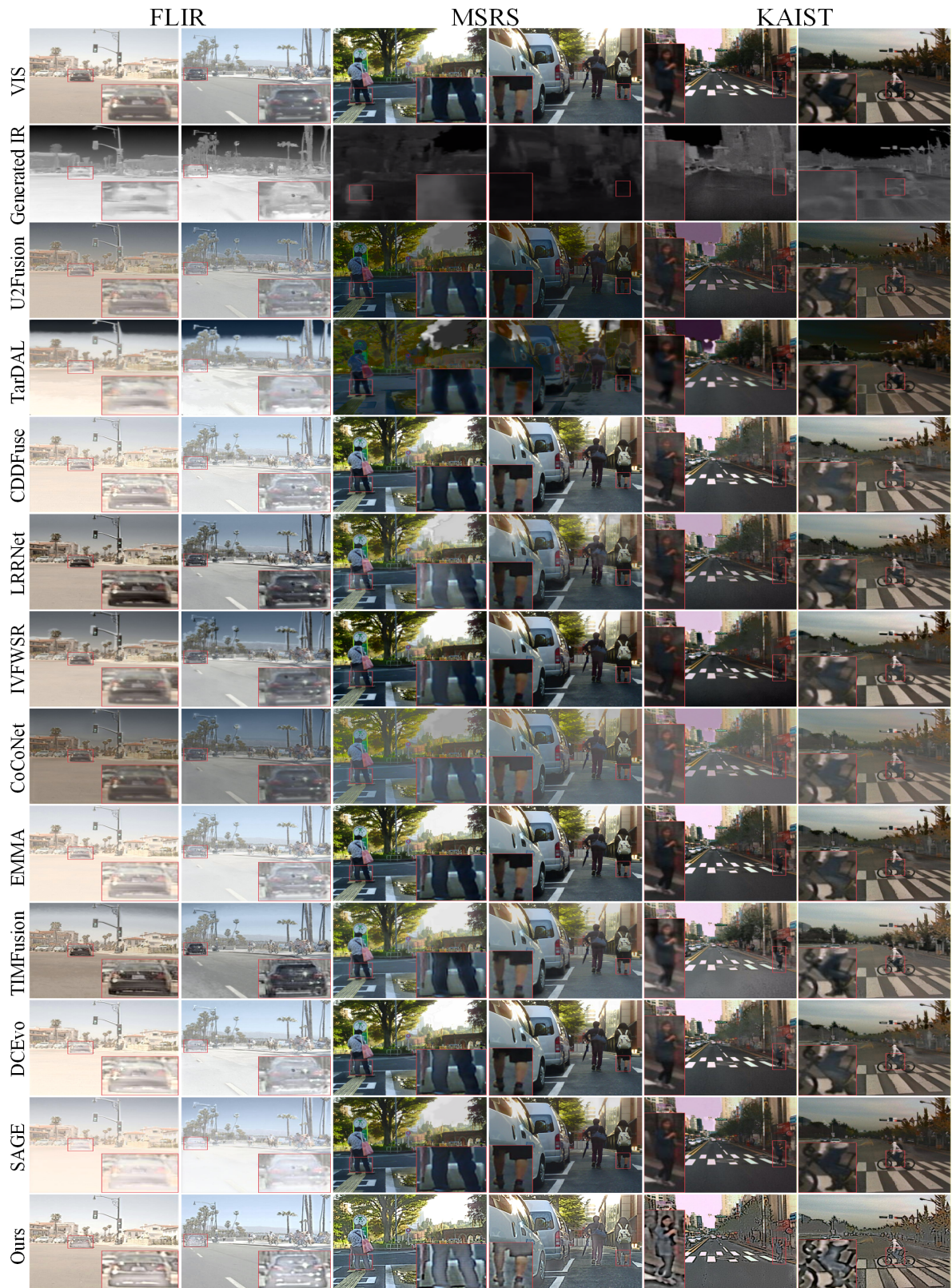


Figure 9. Visual comparison of different fusion methods on the FLIR, MSRS, and KAIST datasets, where the infrared images are generated from visible images using the PID method.

Table 8. Quantitative comparison of different fusion methods on the FLIR, MSRS, and KAIST datasets, where the infrared images are generated from visible images using the EGGAN method. The best and second-best performances are highlighted with Red and Blue backgrounds, respectively.

Datasets	MSRS						FLIR						KAIST					
	AG ↑	CE ↓	EI ↑	EN ↑	Qcb ↑	SF ↑	AG ↑	CE ↓	EI ↑	EN ↑	Qcb ↑	SF ↑	AG ↑	CE ↓	EI ↑	EN ↑	Qcb ↑	SF ↑
U2Fusion	3.289	3.309	34.980	5.447	0.327	9.310	2.320	1.453	24.107	5.045	0.368	6.517	2.425	2.734	25.699	5.489	0.388	6.259
TarDAL	3.205	3.458	34.550	6.640	0.363	8.602	2.341	2.756	25.123	6.536	0.304	6.898	1.916	1.728	20.399	6.197	0.382	5.807
CDDFuse	3.644	2.839	38.606	6.513	0.318	11.581	3.004	0.515	31.810	6.406	0.429	8.746	2.944	4.315	31.419	6.225	0.374	8.835
LRRNet	3.979	4.924	42.225	6.617	0.340	12.258	3.905	1.993	41.323	6.866	0.390	11.946	3.086	2.443	33.250	6.642	0.418	8.862
IVFWSR	3.229	4.218	34.902	6.461	0.378	8.608	3.000	3.704	32.530	6.349	0.422	7.818	2.635	2.631	28.661	6.462	0.414	6.959
CoCoNet	3.930	2.664	41.488	6.312	0.385	11.626	3.948	3.267	41.592	6.363	0.409	11.136	2.716	3.055	28.735	6.006	0.390	7.524
EMMA	4.466	3.236	47.469	6.608	0.366	13.207	3.028	0.691	32.297	6.467	0.427	8.689	3.178	2.969	34.234	6.405	0.414	8.941
TIMFusion	3.887	5.072	41.836	6.839	0.356	11.165	3.892	2.938	41.172	6.571	0.396	11.900	3.479	2.473	37.688	6.894	0.446	9.279
DCEvo	4.170	4.718	44.500	6.814	0.308	13.240	3.246	0.591	34.602	6.532	0.432	9.768	3.451	4.359	37.032	6.628	0.375	9.887
SAGE	4.150	3.057	44.114	6.777	0.327	12.560	2.724	1.160	28.303	5.966	0.403	8.138	3.376	2.986	35.924	6.608	0.430	9.534
Ours	5.037	3.142	53.168	7.188	0.454	14.898	4.518	0.596	48.784	6.639	0.435	12.554	4.414	2.227	37.115	7.073	0.405	11.031

Table 9. Quantitative comparison of different fusion methods on the FLIR, MSRS, and KAIST datasets, where the infrared images are generated from visible images using the PID method. The best and second-best performances are highlighted with Red and Blue backgrounds, respectively.

Datasets	MSRS						FLIR						KAIST					
	AG ↑	CE ↓	EI ↑	EN ↑	Qcb ↑	SF ↑	AG ↑	CE ↓	EI ↑	EN ↑	Qcb ↑	SF ↑	AG ↑	CE ↓	EI ↑	EN ↑	Qcb ↑	SF ↑
U2Fusion	3.074	1.668	32.810	6.047	0.428	9.168	3.277	1.353	33.900	6.576	0.388	8.329	2.533	0.828	27.040	6.180	0.459	6.911
TarDAL	1.938	2.342	20.524	6.030	0.378	5.654	2.516	0.643	26.795	7.055	0.282	6.860	1.937	1.268	20.667	6.302	0.427	5.766
CDDFuse	4.821	1.651	51.500	7.191	0.466	14.142	3.837	0.726	39.804	6.517	0.403	10.254	3.349	1.361	35.909	7.064	0.488	9.859
LRRNet	3.815	2.837	40.509	7.049	0.445	11.150	3.970	1.798	42.038	6.955	0.408	11.154	3.125	1.432	33.685	7.017	0.439	8.740
IVFWSR	3.994	1.342	43.035	7.046	0.470	11.054	2.976	1.266	31.999	7.180	0.377	7.546	2.878	0.857	31.010	6.962	0.442	8.313
CoCoNet	3.357	0.801	35.271	6.477	0.418	10.386	2.456	1.848	25.333	6.417	0.433	6.589	2.200	1.073	23.195	6.240	0.456	6.444
EMMA	4.904	1.353	52.540	7.187	0.440	14.253	3.150	0.745	33.517	6.280	0.390	8.830	3.334	0.813	36.033	6.979	0.495	9.655
TIMFusion	3.952	3.928	42.063	6.936	0.374	11.708	3.967	1.541	42.121	6.982	0.404	11.572	3.430	1.877	36.806	7.004	0.434	9.509
DCEvo	4.722	1.983	50.492	7.231	0.476	13.974	3.468	0.812	36.719	6.531	0.412	9.516	3.439	1.209	36.676	6.998	0.497	10.381
SAGE	4.447	1.867	47.126	7.005	0.436	13.246	2.690	0.697	27.959	6.379	0.339	7.818	3.234	1.035	34.370	6.805	0.416	9.574
Ours	5.037	3.142	53.168	7.188	0.454	14.898	4.518	0.596	48.784	6.639	0.435	12.554	4.414	2.227	37.115	7.073	0.405	11.031